A Method for Obtaining Surface Flow Vectors and Its Implementation in Interferometric Skin Friction Measurement

Mehti Koklu*, Dan H. Neuhart†, Latunia P. Melton ‡
NASA Langley Research Center, Hampton, VA, 23681, USA

Jonathan W. Naughton§
University of Wyoming, Laramie, WY, 82071, USA

A new method was developed to extract surface flow vectors from an oilflow visualization image that has oil streaklines. The method is analogous to the PIV processing where the image is divided into interrogation windows. A representative flow direction is obtained for each interrogation window using image processing with a line-detection algorithm. Repeating the process for the entire image, one can find the surface vector field. The Hough transformation, Radon transformation and Machine Learning were used as line-detection algorithms. The obtained vector field is then postprocessed to filter spurious vectors and to apply smoothing. The method was tested on 2D and 3D models with different flow complexities. The method was able to predict surface flow vectors for all cases tested. The predicted surface flow vectors were used in obtaining the surface skin friction. The successful implementation of the surface flow vectors enables interferometric skin friction measurements on surfaces beneath 3D complex flows. In addition, the surface flow vectors can be superimposed on the oilflow visualization images to better explain the surface flow topology.

I. Introduction

The motion of an oil film provides valuable information about the flow it is subjected to. Because of an oil film's relatively small thickness, it is usually considered as nonintrusive to the flow. There are many techniques that use the motion of oil film to aid in understanding complex three dimensional (3D) fluid flows. One well-known application of oil film is the surface oilflow visualization. Surface oilflow visualization (OFV) is a qualitative technique that involves the application of oil with fluorescent dye or pigment to the region of interest [1]. Overall surface flow topology can be obtained using OFV including flow separation and flow reattachment.

Another well-known application of oil film is the measurement of surface skin friction using interferometric techniques. A comprehensive review of the oil flow interferometry (OFI) skin friction measurement is given by Naughton and Sheplak [2]. Skin friction measurement using OFI involves the solution of the thin oil film equation, which was first described by Squire [3]. Later, Tanner and Blows [4] implemented the thin oil film equation in the skin friction measurement. Assuming an oil droplet on a surface, the thickness of oil, $\boldsymbol{h}$, gradually reduces under the effect of shear stress (Fig. 1). Using the mass flow conservation law, Tanner and Blows obtained the following relation [4]:

$$h(s,t) = \frac{\mu}{t\sqrt{\tau_w n}} \int_0^s \sqrt{n/\tau_w}\,.\,ds, \tag{1}$$

---

* Research Scientist, Flow Physics and Control Branch, MS 170, AIAA Member
† Research Scientist, Flow Physics and Control Branch, MS 170
‡ Research Scientist, Flow Physics and Control Branch, MS 170, AIAA Associate Fellow
§ Professor, Mechanical Engineering Department, AIAA Associate Fellow

where $\boldsymbol{\mu}$ is the oil dynamic viscosity, $\boldsymbol{s}$ is the distance along the streamline, $\boldsymbol{t}$ is the time to travel the distance $\boldsymbol{s}$, and $\boldsymbol{n}$ is the spacing between two limiting streamlines, $\boldsymbol{s_1}$ and $\boldsymbol{s_2}$. Note that when the flow is uniform, the streamlines are linear lines, and $\boldsymbol{n}$ becomes constant and cancels out in this equation. Since the oil viscosity could vary depending on the model temperature during the tunnel run, a more generalized form of this equation can be used to find the shear stress [5]:

$$\sqrt{\tau_w} = \int_0^s \sqrt{n/\tau_w}\,.\,ds/h(s,t)\sqrt{n}\ \int_0^t \frac{dt}{\mu}. \tag{2}$$

This expression does not have an explicit solution; therefore, an iterative approach can be used. The nondimensional skin friction coefficient can be calculated by using the dynamic pressure [2].

$$\sqrt{C_{f,i+1}} = \int_0^s \sqrt{n/C_{f,i}}\,.\,ds/h(s,t)\sqrt{n}\ \int_0^t \frac{q}{\mu}.\,dt \tag{3}$$

As shown in this equation, the skin friction requires the time dependent thickness of oil film along the streamline, $\boldsymbol{h(s,t)}$. The oil film thickness can be measured using the interferometry techniques; however, Eq. (3) also requires local flow streamlines and the spacing $\boldsymbol{n}$. This requirement of local flow direction is possibly one of the main limitations of the OFI measurement's usage in complex 3D flows. Several methods have been developed in the literature for this purpose. Recently, Baldwin et al. [6] used a cross-correlation-based methodology (i.e., particle image velocimetry, PIV) to compute local flow direction. In the absence of seeding particles in the oil mixture, a series of differential images were used in the PIV processing. These differential oilflow images were created by subtracting the prior image from each successive image, and the relative motion of the oil mixture acted as seeding particles. In another study, Lunte et al. [7] presented a heuristic approach where a set of streamlines were hand drawn, and additional streamlines were interpolated using these limited set of hand-drawn lines.

Motivated by the requirement of surface flow streamlines in the OFI skin friction measurement technique, especially for 3D complex flows, the objective of this research is to develop a method to obtain surface flow vectors. The surface flow vectors not only enable OFI measurements in complex flows, but also improve the understanding of oilflow visualization when the flow vectors are superimposed onto oilflow visualization images.

II. Experimental Setup and Methodology

Most of the experiments were conducted in the NASA Langley 20-Inch by 28-Inch Shear Flow Tunnel. The primary model used in this study is the NASA wall-mounted hump model, which was used as a benchmark case for computational fluid dynamic (CFD) validation. The detailed description of the model and the wind tunnel can be found in Ref. [8]. The experiments were conducted at a freestream Mach number of 0.1, which corresponds to a Reynolds number of 0.94×10^6 based on the hump chord length, $\boldsymbol{c}$ = 420 mm. Additional testing was also performed in the NASA Basic Aerodynamic Research Tunnel (BART) with a 3D flow configuration (30° swept NACA 0015 model).

The baseline flow over the hump model is given in Fig. 2. The simulated surface flow visualization [9] is presented here to show the overall flow topology before explaining the surface flow vector extraction method. Near-surface streamlines are superimposed onto the contours of velocity magnitude to show the three-dimensional flow. Note that the endplates are removed in this figure in order not to block the view. The flow separates near x/c = 0.66. Flow separation is nominally two-dimensional except near-endplate regions due to the corner vortices. The flow reattaches at x/c = 1.266 in this CFD simulation, and attached flow is observed downstream. The flow reattachment region provides rich flow features such as reattachment node, attached flow, reversed flow, and converging and diverging streamlines.

A. Surface Oilflow Visualization

Surface oilflow visualization is commonly used as a qualitative technique to show overall flow topology. An oilflow visualization image can also be postprocessed to determine the flow separation and reattachment locations. The surface oilflow visualization technique involves applying a mixture of oil on the surface of interest. The most important parameter is the oil viscosity since you do not want oil to be moved by the shear stress too quickly nor too

slowly. Another requirement in the oil mixture is the availability of pigment or dye such that it will be seen visually or with the camera. There are many oil mixtures and recipes for oil mixture in the literature. One of the most common mixtures is kerosene and TiO_2. In this case, the kerosene oil is the carrier fluid and TiO_2 particles serve as pigment and also modify the viscosity of the mixture.

A typical surface oilflow visualization is presented in Fig. 3 for the separated flow over the NASA hump model [10]. This OFV was obtained using a mixture of aviation oil, kerosene, and nano-silica particles. Details of this oilflow visualization technique can be found in Ref. [11]. The flow direction in this OFV image is from top to bottom. Two small corner vortices are observed downstream of the separation line at each side. The separation line is essentially two dimensional with the exception of the near-endplate regions. The flow reattachment is fairly uniform around the centerline; however, the reattachment points move upstream closer to each corner vortex. Each corner vortex generates a reattachment node, where one can see oil movement in all directions. The oilflow visualization image was postprocessed to find the flow separation and reattachment locations. The separation location was found to be at x/c = 0.66. The average reattachment location around the centerline is x/c = 1.15. When compared to the surface flow visualization obtained by CFD simulations in Fig. 2, key flow features such as flow separation, flow reattachment, reattachment nodes, and corner vortices compare well.

Another surface OFV technique was recently introduced in the literature [12], which has certain advantages that experimentalists will appreciate. The main advantage is that this OFV technique provides surface oil streaklines. The technique involves spreading nonfluorescent oil (e.g., silicone oil) of desired viscosity on the surface using a regular paint brush or a roller. The oil can sit for a longer period of time since the oil does not have any volatile compound (such as kerosene or other carrier fluid). In fact, the waiting time helps the oil to smooth out on the surface without any brush strokes. In addition, oil will spread on the surfaces more uniformly, although nonuniformities do not show up in the OFV images.

After spreading the oil, fluorescent particles are applied over the oil layer. The fluorescent particles are in powdered form and can be applied using a shaker. This is somewhat counterintuitive to the typical oilflow visualization where we usually mix oil and fluorescent particles then apply the mixture on the surface of interest. In this new technique, the powdered particles are sprinkled onto the oil layer. These particles act as seeding or initial points for the oil streaklines. Since the fluorescent particles can be seen under the room light, the uniformity can be visually checked during the application process, and more particles are applied if necessary. The uniform distribution of powdered particles is also analogous to PIV where we usually try to get a uniform seed particle distribution in an interrogation window and throughout the field of view.

A sample image of the particle distribution is seen in Fig. 4a. The image is taken with a UV light source using a digital camera mounted on the tunnel. The location corresponds to Location 1 in Fig. 2, which is near the suction peak of the hump model. The individual particles are clearly seen and resemble the seed particles in a PIV plane. Although oil is also applied, it does not show up in the image as the oil does not contain any fluorescent dye.

When the tunnel is turned on, the shear stress moves the oil. It was noted that the powdered fluorescent particles mostly stay in place while oil is moving under the shear stress. The oil passing the fluorescent particles entrains some of the fluorescent pigment and forms individual streaklines (Fig. 4b). As shown in CFD (Fig. 2), the flow at this location is uniform and two dimensional. The flow direction is from top to bottom; therefore, the streaklines are straight. Although the flow direction is easy to predict at this location, it can also be determined from a zoomed image by checking the streakline direction compared to the individual particles. Since each streakline emanates from a corresponding seed particle, the streakline direction referenced to the seed particle indicates the local flow direction.

B. Surface Flow Vector Extraction Method

The surface flow vector extraction (SFVE) method is initially developed and tested using simple 2D attached flow over the Location 1 in Fig. 2. The SFVE method was motivated by PIV processing. PIV requires an image pair that have sufficient particle movement between the first and the second image frames. Typically, the time lapse between two images is very small; therefore, PIV indicates a very short time integral and basically captures instantaneous displacements. On the other hand, the current SFVE method requires a single OFV image with oil streaklines (i.e., sufficient oil movement). These streaklines carry the time history of surface flow information and indicate a very long time integral.

In the PIV procedure, first, the image is divided into interrogation windows. Then, a cross correlation algorithm is used to determine a common (or most probable) displacement, Δx, of the particles from the first image frame to the second image frame (Fig. 5). Since the Δt between two images is known, one can calculate a common velocity, $\Delta x/\Delta t$, for each interrogation window. In a similar manner, the OFV image is divided into interrogation windows in the current SFVE method. The aim is to find a common or most probable flow direction for each interrogation window.

The representative flow direction for each interrogation window is obtained by finding the common direction of the streaklines in an interrogation window using a line-detection algorithm in digital image processing (Fig. 6).

There are various line-detection algorithms in digital image processing. Two well-known techniques are the Hough transformation and the Radon transformation. In addition to these mathematical methods, Convolutional Neural Networks (or Machine Learning) can be used for line detection as well.

1) Hough Transformation

The Hough transformation is a feature extraction (line detection) technique used in many fields related to the digital image processing and computer vision. The Hough transform was first invented by Hough [13] to recognize complex patterns but its current form was developed by Duda et al. [14]. Although the Hough transform was initially used to detect lines, its generalized form can be used to detect arbitrary shapes such as circles or ellipses [15]. This technique detects a line by parametric representation of a line in (*x, y*) coordinates in $\rho = x\sin(\theta) + y\cos(\theta)$ form, where $\boldsymbol{\rho}$ is the distance to the origin and $\boldsymbol{\theta}$ is the angle between the line and *x*-axis. The Hough transformation generates a parameter space matrix that is composed of $\boldsymbol{\rho}$ and $\boldsymbol{\theta}$ values. The peak values of the parameter space matrix represent the potential lines in the input image.

Assume we have an input image that consists of three lines as in Fig 7a. The angles between the lines and *x*-axis are 0°, 30°, 75°, respectively. Note the origin is located on the upper left corner and the *x*-axis is the vertical direction. When the Hough transformation is applied, the peak points in the $\boldsymbol{\rho}$ - $\boldsymbol{\theta}$ contour plot exactly correspond to the angles of three lines in the input image (Fig. 7b). The negative sign is due to the fact that the angle is measured in the clockwise direction in the Hough algorithm. As such, the Hough transformation could be used to identify the oil streakline angle and hence the vector direction in an interrogation window. Here we are only interested in $\boldsymbol{\theta}$ values as we are looking for the vector direction in an interrogation window and not interested in the $\boldsymbol{\rho}$ values (i.e., the distance of the line to the image center).

The SFVE method is implemented as follows: First, the OFV image (Fig. 8a) is converted to a grayscale image (Fig. 8b) and divided into interrogation windows. Then an edge detection algorithm (such as Canny edge detection method) is used to detect edges (Fig. 8c). The Hough transformation is then applied to detect lines (i.e., streaklines) in the interrogation window (Fig. 8d). The Hough transformation provides the angles ($\boldsymbol{\theta}$) of the potential lines. The flow direction angle for the current interrogation window is obtained by averaging the angles. The process is repeated for the entire image to find the surface flow vector field. It should be noted that the SFVE method provides only local flow direction (i.e., angle) not the magnitude; therefore, the computed vectors have unit vector length.

The surface flow vectors obtained using the OFV image in Fig. 4b are presented in Fig. 9. The flow in this region is two dimensional, where the flow direction is from top to bottom. The OFV image was divided into 48 pixels by 48 pixels interrogation windows with 50% overlap. Using the procedure described, the extracted surface flow vectors are shown in Fig. 9a. As noticed, the flow vectors are mostly from top to bottom. The vector field includes spurious vectors due to limited information (i.e., limited image intensity to form a line).

Similar to PIV processing, one can use a postprocessing algorithm to filter and smooth the flow vectors. Although any PIV postprocessing (either commercial or academic) could be used to postprocess the vectors, the postprocessing algorithm developed by Garcia et al. [16] was used in this study. This postprocessing algorithm uses the spline technique, and the source code is available as supplementary material on the publisher's website [16]. Applying the postprocessing technique to the raw data resulted in a smooth vector field (Fig. 9b). As expected, all flow vectors point down showing a two-dimensional flow field where the flow direction is from top to bottom.

2) Radon Transformation

Another popular method for line detection is the Radon transform. The Radon transformation is widely used in many fields, especially in medical tomography [17]. It was shown that the Radon transform is equivalent to the continuous form of Hough transformation [18]. The Radon transformation represents the projection of $\boldsymbol{f(x,y)}$ function onto the $\boldsymbol{x'}$-line as $\boldsymbol{R(x')}$. In image processing, it is the projection of the image intensity along a radial line, $\boldsymbol{x'}$, oriented at a specific angle, $\boldsymbol{\theta}$ (Fig. 10a). The integral of $\boldsymbol{R(x')}$ is computed for each $\boldsymbol{\theta}$, and the $\boldsymbol{x'}$-line with the largest integral value represent the possible line in the image. Applying the Radon transformation to the same input image in Fig. 7a, we obtain a contour plot that is given in Fig. 10b. Similar to that of the Hough transformation, the peak points correspond to the angles of the lines. Note that $\boldsymbol{\theta}$ is the angle from *x*-axis and measured in the counterclockwise direction; therefore, the angle values are positive.

The SFVE procedure is similar to that with the Hough transform: first, the OFV image is converted to a grayscale image and divided into interrogation windows. In this method, we do not use an edge detection algorithm but apply Radon transformation to the grayscale image. Since Radon transformation computes the integrals along the $\boldsymbol{x'}$-lines,

each line at different orientations has a different length for a rectangular interrogation window (see $\boldsymbol{x_1'}$ and $\boldsymbol{x_2'}$ lines in Fig. 11a). This causes large erroneous integral values especially near ±45°. Therefore, one has to use a circular interrogation window to have similar lengths for all $\boldsymbol{x'}$-lines. A circular interrogation window can be implemented by applying a circular mask to a rectangular interrogation window as shown in Fig. 11b. When the Radon transformation is applied to the masked image, the angle of the largest integral will be the most probable angle that represents the streakline in the interrogation window, hence the flow direction. The process is repeated for the entire image to find the surface flow vector field. At the end, a PIV postprocessing algorithm is used to filter and smooth the vector field.

3) Convolutional Neural Networks

The third method that is used as a line-detection algorithm is supervised Machine Learning (ML), which uses convolutional neural networks (CNN). ML is a powerful tool for object detection that is commonly used in detecting road lanes for self-driving or advanced driver-assistance system equipped vehicles (Fig. 12a). Since our aim is to detect lines in an interrogation window, ML is a perfect candidate for this application (Fig. 12b). Details of the ML and CNN algorithms will not be discussed here since we used ML as a tool or a black box, where we were only interested in the inputs and outputs without detailed knowledge of the internal workings. There are many different CNN algorithms that can be used for line detection. Therefore, it is expected that different CNN algorithms would result in different accuracy, cost, etc. when obtaining the surface flow vectors. The purpose here is to show the potential of using ML in the SFVE method.

Since ML is used as a black box, we picked a CNN algorithm that was used in an approach that is close to the current application. One such application is the particle streak velocimetry using CNN by Grayver et al. [19]. The CNN algorithm was written using the PyTorch libraries, and the Jupyter notebook version of the source code is available in Ref. [20]. Particle streaks can occur during PIV image acquisition when the exposure time is long relative to the particle motion. The particle streaks are undesired in PIV because the cross-correlation algorithms may not work efficiently. The particle streak velocimetry using CNN was developed as an alternative to the cross-correlation algorithm for the cases where the particle streaks are inevitable. However, in our case, since we are using the oil streaks to find surface flow direction, this implementation of CNN algorithm is a perfect fit. The main challenge of using any CNN is the availability of a sufficient training dataset. Using DNS data, authors generated millions of images by randomly varying intensity, thickness, and number of streaks in each image [19]. Out of this dataset, 75% was used in training and 25% was used in validation. Referring details of the CNN algorithm to the reference paper [19], a summary is provided here: The ensemble network consists of 10 networks with the same architecture and parameters. Each network has four convolutional units with increasing depth, followed by a 30% dropout, and a fully connected (FC) layer at the end. Each convolutional unit consists of a 2D convolutional layer, activation layer (rectified linear unit), average pooling layer, and a batch normalization layer (Fig. 13).

The SFVE procedure is similar to the one with the Hough transformation. The OFV image is converted into grayscale and an edge detection algorithm is applied to the image. This image is provided to the CNN algorithm where the CNN algorithm divides the image into interrogation windows. The ensemble network is applied to the image, and the resulting vector field is obtained by averaging the results of 10 networks. The CNN algorithm provides the length and orientation angle of the streaks for each interrogation window, where the orientation angle is converted the flow direction. At the end, a PIV postprocessing algorithm is used to filter and smooth the vector field.

C. Implementation of Surface Vectors in OFI Skin Friction Method

Once the surface flow vectors have been obtained, surface streamlines can be calculated. The process is summarized in Fig. 14. First, spatial calibration images are taken for the images from which the surface flow vectors were determined. These calibration images are used to calibrate the camera system using an approach that was described by Naughton and Liu [21]. This step is necessary so that the locations in the images used to determine the surface flow vectors can be associated with the locations on the model surface. A similar process is also performed on the oil film interferometry images so that a common coordinate system is determined from images taken from different camera locations and orientations. An example result is shown in Fig. 15 for a 3D model (NACA 0015 sweptback wing), where the surface oilflow visualization image (Fig. 15a) and interferogram image (Fig. 15b) are overlaid with lines of constant x and y coordinates. Notice that these images have been taken with two different camera settings (e.g., different camera locations, orientations, etc.). The camera zoom level or field of views are also different such that the oil-film interferometry image occupies a small region in the oilflow visualization image. Using this information, any location in the image (i, j) may be associated with its physical location on the model (x, y, z), and the surface streamline direction (Δi, Δj) is converted into its direction in model coordinates (Δx, Δy, Δz). With the locations of the surface flow vectors known, a starting point may be chosen, and the surface flow vectors are integrated using small steps to determine the surface streamlines.

In this effort, the motivation behind determining these streamlines is to identify the path along which thin oil films flow. These streamlines are used along with oil film interferometry images taken in the same flow under the same conditions to identify the paths in the interferograms to analyze. Once these paths are known, typical oil-film interferometry analysis methods (e.g., Naughton and Liu [21] and Naughton et al. [22]) may be used even in flows with complex surface flows. Although a similar approach has been applied to flat surfaces (see Baldwin et al. [6]), the analysis here is extended to 3D surfaces with curvature.

III. Results

A. Surface Flow Vectors Over a Complex Region

The flow vectors extracted in Fig. 9 indicate the feasibility of the SFVE method. As presented in Fig. 2, the flow over this region is two dimensional and uniform. For uniform flows, the spacing between limiting streamlines, $\boldsymbol{n}$, is constant and cancels out in Eq. (3). Therefore, OFI skin friction measurement may not require limiting streamlines in this region as the fringe patterns can be calculated on the vertical lines. The next step was to test the SFVE method in a more complex flow region (e.g., Location 2 in Fig. 2). As shown in the CFD simulation (Fig. 2), the flow in this region contains a reattachment node that results in a very complex 3D flow field consisting of reversed and attached flows with converging and diverging streamlines. Figure 16a shows the surface oilflow visualization obtained at this location. The oil streaklines together with the individual fluorescent particles are seen in the image.

Using this OFV image, the SFVE method with Hough transform produced the surface vector field presented in Fig. 16b (only every 4th vector is plotted). Overall, the surface flow vectors closely follow the oil streaklines. The flow directions inside the separated flow region (enclosed by the polygon) are found to be incorrect (i.e., not showing reversed flow), although the vectors follow the oil streaklines. This is because there is 180° ambiguity in the flow direction because the line-detection algorithm only detects lines not directions. This is not a limitation of a particular line-detection algorithm because a line segment inside an interrogation window does not have the information of the starting point. The 180° ambiguity in the flow direction is independent of the algorithm and was also seen in the particle streak velocimetry [19]. As shown in this figure, these incorrect vectors are not randomly distributed in the vector field but occur when the flow direction changes. In this particular case, the streamwise component of the velocity changes sign due to flow separation. Since we know the overall flow field, the flow direction in this region can be corrected by flipping the direction angles (i.e., adding π to the orientation angles). For the cases that the overall flow field is not known, the local flow direction can be found by checking the oil streaklines. Since each streakline emanates from a corresponding seed particle, the streakline direction referenced to the seed particle indicates the local flow direction. The corrected surface flow vectors are presented in Fig. 17a. The vector field includes spurious vectors, which can be filtered using the PIV postprocessing algorithm. The postprocessed surface flow vector field (every 4th vector is shown) is presented in Fig. 17b. The surface vector field obtained using the oilflow visualization is very similar to that obtained from CFD simulations (Fig. 2) thereby confirming the applicability of the SFVE method to complex 3D flows.

Next, the same OFV image in Fig. 16a is processed using the Radon transformation to find the surface flow vectors. As presented in Fig. 18a, the surface flow vectors closely follow the oil streaklines. Similar to the Hough method, there is 180° flow direction ambiguity. This time the flow directions on the right-hand side of the figure are incorrect where the spanwise component of the velocity changes sign at the centerline. Again, these incorrect flow vectors are corrected by flipping the flow direction angles. Note that the flow direction angles were incorrect in the separated flow region for Hough transform whereas it is on the right-hand side of the figure. Without knowing the exact reason, it is possibly due to the fact that Hough transformation is defined between $\{-\pi/2 - \pi/2\}$, and the angle is measured in clockwise direction whereas the Radon transformation is defined between $\{0 - \pi\}$, and the angle is measured in counterclockwise direction.

Lastly, machine learning is used to extract the surface flow vectors using the same OFV image in Fig. 16a. The surface flow vectors obtained using the CNN algorithm are shown in Fig. 19a. Overall, the flow vectors follow the oil streaklines for most of the region. Similar to the Radon case, the flow vectors are incorrect on the right-hand side of figure where the spanwise velocity component changes sign at the centerline. These vectors are corrected by flipping the flow direction angle. The CNN algorithm was unable to predict the flow vectors accurately near the centerline. The vectors near the centerline are not random spurious vectors but they are inaccurate. As shown in the OFV in Fig. 16a, we have 2D flow near the centerline where we expect straight flow vectors as predicted by two previous methods. However, the CNN method systematically predicted lateral flow. As presented earlier in Fig. 13, the CNN algorithm consists of 10 CNN layers, and the final vector field is the average of these 10 vector fields obtained by each CNN layer. We can also use the results of 10 vector fields to calculate the standard deviation of the predicted angles. As

shown in Fig. 19b, the standard deviation of the predicted flow directions is as large as 45° near the centerline. In addition to the near centerline regions, the standard deviations on the upper left and lower right of the OFV image are large where information (the number of oil streaks) is limited. The standard deviation data can be used to filter the vector field. The result is presented in Fig. 20a where the vector field is filtered out based on the standard deviation and postprocessed using the PIV postprocessing algorithm. The obtained surface flow vectors closely follow the oil streaklines and provide a similar vector field to the two previous methods.

Figure 20b compares the vector fields obtained using three line-detection algorithms where the vector fields are superimposed on the OFV image. The vector fields obtained by the Hough and Radon transformations match perfectly and lie on top of each other. The differences (yellow vectors) only appear over the limited regions where we do not have sufficient oil streaks. The CNN results agree reasonably with others for most of the regions. The differences (red vectors) appear mostly near the centerline where the vectors were filtered using the standard deviation of direction angle (Fig. 19b) and the PIV postprocessing algorithm filled the vector field. The other differences (red vectors) appear over the regions with limited oil streak information.

Although the CNN algorithm result deviates from the results of the Hough and Radon transformations, this does not indicate a weakness or deficiency of CNN in the surface flow vector extraction method. It should be noted that the current CNN algorithm was not developed for oil streakline detection. In addition, the streak data that were used in training the CNN model do not represent the oil streaklines. Most importantly, the maximum streak length was assumed to be less than half the window size in the CNN algorithm. In fact, the CNN model systematically resulted in incorrect predictions for the streak lengths larger than the half window size in the particle streak velocimetry [19]. This assumption was frequently violated in our case as the continuous oil streaklines usually have lengths larger than the half window size. Despite the inaptness, the CNN algorithm was able to predict a surface flow vector field that is comparable to those of the Hough and Radon transformations. With a more suitable CNN algorithm and training dataset that is representative of oil streaks, there is great potential in CNN algorithms for extracting surface flow vectors using the OFV images.

B. Surface Flow Vectors On The NACA0015 Airfoil

Next, the SFVE method was tested on a 3D flow configuration. The wind tunnel model is an NACA 0015 semispan wing with 0.3048 m chord and 0.68 m span (Fig. 21). The model has a leading edge sweep of 30 degrees and tested in the NASA Langley Research Center Basic Aerodynamics Research Tunnel. Detailed information about the model and wind tunnel can found in Ref. [23]. The model has a 30% chord trailing edge flap; however, the flap was undeflected during the testing of the SFVE method. Experiments are conducted at a freestream Mach number of 0.1, which corresponds to a Reynolds number of 0.75×10^6 based on the wing chord. The model was tripped near the leading edge of the wing to provide a turbulent boundary layer over the wing upper surface. The model has several surface pressure ports (see dots in Fig. 21) that were covered with tape during OFV experiments. Our area of interest is a 10-inch-wide region near the midspan of the model. The model surface in this region was covered with two 5-inch-wide mylar strips on each side of the centerline pressure ports.

Figure 22a shows the surface oilflow visualization for an angle of attack of 8°. Note that the image is rotated such that the leading edge of the model appears horizontal. When rotated, the freestream flow is angled 60° to the leading edge of the model as shown by the arrow. At this angle of attack, flow is usually attached both on the main element and on the flap. However, the surface OFV shows flow separation near the leading edge of the flap. This is caused by the small step between the trailing edge of the main element and the flap. The original wind tunnel model was built for active flow control testing; therefore, the step was required for blowing from the flap shoulder. The flow appears to reattach on the flap surface and remains attached afterward. The oil streaklines not only appear in the attached flow region but also in the separated flow region and indicate reversed flow.

This OFV image is used to extract surface flow vectors using the methods described earlier. Surface flow vectors obtained using three different line-detection algorithms were superimposed on the OFV image (Fig. 22b) to highlight the differences. As shown, the surface flow vectors closely follow the oil streaks showing attached flow both on the main element and on the flap and the separated flow near the leading edge of the flap. Similar to the previous cases, the vectors obtained with Radon and Hough transformations agree very well and lie mostly on top of each other. There are a few spots where we are able to see the yellow vectors (i.e., differences) due to the insufficient oil streaklines. The vector field obtained by the convolutional neural networks (red vectors) appears in most of the regions indicating that the agreement of the vector fields is not perfect although the flow topology is similar. The disagreement is more pronounced near the flow separation on the flap leading edge. Given the good agreement between the Hough and Radon transformations, this discrepancy is not due to OFV and the oil streaklines but possibly due to the present CNN algorithm's limitations to be applied for streakline detection. Despite the differences, the vector field obtained by the CNN characterizes the flow and represents the overall flow topology over the wing.

When the angle of attack is increased ($\alpha = 14°$), the sweep effects are more pronounced on the flow field. As shown in the surface OFV (Fig. 23a), we see stronger spanwise flow on the main element. The flow appears attached on the main element, however, the entire flow over the flap is separated. The flow separation is different than that of the $\alpha = 8°$ case. While flow separation is followed by flow reattachment and caused by the step in the $\alpha = 8°$ case, in this case it is 3D flow separation without flow reattachment and mainly caused by the interaction of the adverse pressure gradient and the wing sweep. Oil streaklines are present in most of the regions except near the inboard side of the flap. Since the flow is approaching separation, lower magnitude shear stress could not generate sufficient oil movement.

Surface flow vectors obtained using the OFV image ($\alpha = 14°$) are presented in Fig. 23b. Again, all three vector fields are superimposed on the OFV image to highlight the differences. The vector fields obtained by the Hough and Radon transformations agree very well except for a few spots possibly due to the insufficient oil streaklines. Although the agreement between the CNN and other methods is better than the $\alpha = 8°$ case, the appearance of red vectors especially over the flap indicates slight disagreement between the CNN and other two methods. There appears to be an anomaly in the flow vectors near the midspan over the flap where there are a few vectors pointing down. A close investigation revealed a surface irregularity on the trailing edge of the main element. This surface irregularity acted as a vortex generator and delayed flow separation at this particular location. This effect was also visible in the $\alpha = 8°$ case, where there is a slight change in the flow pattern.

C. Skin Friction Measurement On The NACA 0015 Airfoil

The next step is to demonstrate the measurement of the surface skin friction for a complex 3D flow with the help of the surface flow vectors. For this pupose, flow over the NACA 0015 sweptback wing at $\alpha = 14°$ is considered. As presented in Fig 23, this case shows a complex flow field with 3D flow separation. The implementation method described in the analysis section are applied to oil-film interferometry images taken on the NACA 0015 wing at $\alpha = 14°$. The complex flow at this angle (Fig. 23) demonstrates the need for the approach developed here. Figure 24a shows the surface flow vectors overlaid on the oil film interferometry image. Note that Fig. 24a corresponds to a small region in Fig. 23 as the camera settings, especially the zoom level, are completely different. Using the approach discussed in the analysis section, a starting point on the surface is selected (the circles in Fig. 24b) depending on the desired skin friction measurement location. The surface streamlines are determined using the surface flow vectors shown in Fig. 24b. Only the vector field obtained using the Hough transformation is presented here for demonstration purposes. It is important to stress that coupling of the surface flow vectors and the interferograms is only possible through rigorous camera calibrations.

Once we obtained the surface streamlines, the remaining quantity to determine is the surface skin friction. This can be done by processing of the intensity profiles along the streamlines shown in Fig. 24b. The intensity profile comprises the interference patterns (peaks and valleys), which can be analyzed to determine the local oil film thickness. Using the local oil film thickness, the tunnel dynamic pressure, and oil viscosity, the solution of Eq. (3) along the streamline results in surface skin friction values. Figure 25 presents the measured skin friction values along these streamlines. As can be seen, the skin friction varies along both the chord and span of the wing model as expected in this complex flow.

IV. Conclusion

This paper presents a new method that was developed to extract surface flow vectors. The surface flow vector extraction (SFVE) method is based on an oilflow visualization technique, which provides oil streaklines. The method involves postprocessing of a single, long time-averaged oilflow visualization image. The SFVE method is analogous to PIV processing where the image is divided into interrogation windows, and a representative flow direction for each interrogation window is sought. While the PIV processing uses cross-correlation algorithms to find the representative displacement for each interrogation window, the current SFVE method uses line-detection algorithms to find a representative flow direction for each interrogation window. When the process is repeated for the rest of the interrogation windows, one can obtain surface flow vectors for the entire image.

The core of the SFVE method is the line-detection algorithm to detect streaklines for each interrogation window. Two main line-detection algorithms used in the SFVE method are the Hough and Radon transformations. In addition, an existing Convolutional Neural Networks architecture was repurposed to be used as a streakline detection algorithm. After repeating the line-detection algorithm for all interrogation windows, a surface vector field is obtained for the entire image. At the end, a PIV postprocessing algorithm is applied to the vector field to filter and smooth the spurious vectors.

The SFVE method was tested on four flow fields: attached flow over the 2D Hump model, separated flow over the 2D Hump model with a reattachment node, attached flow over a 3D swept NACA 0015 model ($\alpha = 8°$) and flow over a 3D swept NACA 0015 model with 3D flow separation ($\alpha = 14°$). For all cases, the SFVE method with the three line-detection algorithms successfully predicted the surface flow vectors. The agreement between the Hough and Radon transformation results are very good, often the vectors lie on top of each other. The disagreement is rare and only over a few spots where there is limited oil streakline information. The vector field obtained by the CNN appears to be slightly off compared to the other results. However, the deviations do not indicate a weakness of CNN in surface flow vector extraction. The possible reasons for the deviation are twofold: first, the streak data that were used in training the CNN model do not represent the oil streaklines. Second, the maximum streak length assumption in the CNN algorithm was frequently violated when detecting the oil streaklines. Despite the inaptness, the CNN algorithm was able to predict a surface flow vector field that is comparable to the Hough and Radon transformations. With a more suitable CNN algorithm and training dataset, there is great potential in CNN algorithms for extracting surface flow vectors using the OFV images.

The obtained surface vector field is then implemented in the measurement of skin friction using oil flow interferometry. For demonstration purposes, the flow over the NACA 0015 sweptback wing ($\alpha = 14°$) was considered. The surface streamlines were easily calculated using the obtained surface flow vector field. The surface skin friction was measured by oil film analysis of the interferogram profiles along the surface streamlines. The successful implementation of the SFVE method expands the OFI skin friction measurements to complex 3D flows.

Acknowledgement

This work was supported by the Vehicle Systems Integration Subproject of the Advanced Air Transport Technology Project in the NASA Advanced Air Vehicles Program. The second author was funded by the NASA Transformational Tools and Technologies project of the Transformative Aeronautics Concepts Program, and the fourth author was funded through a collaborative agreement through the National Institute for Aerospace with the University of Wyoming (NIA.COOP.03.202085). The authors would like to thank the following individuals for their support; Luther Jenkins, Christal Kellam, and Charlie Debro.

References

[1] Merzkirch W., *Flow visualization*, 2nd ed., Academic Press, New York, 1987.

[2] Naughton, J. W., and Sheplak, M., "Modern Developments in Shear Stress Measurement," *Progress in Aerospace Sciences*, Vol. 38, 2002, pp. 515–570.

[3] Squire, L. C., "The Motion of a Thin Oil Sheet Under the Boundary Layer on a Body," *Flow Visualization in Wind Tunnels Using Indicators*, AGARDograph 70, edited by R. L. Maltby, 1962, pp. 7–23.

[4] Tanner, L., and Blows, L., "A Study of the Motion of Oil Films on Surfaces in Air Flow, with Application to the Measurement of Skin Friction," *Journal of Physics, E: Scientific Instruments*, Vol. 9, March 1976, pp. 194-202.

[5] Garrison, T. J., and Ackman, M., "Development of a Global Interferometer Skin-Friction Meter," *AIAA Journal*, Vol. 36, No. 1, 1998, pp. 62–68.

[6] Baldwin, A., Mears, L. J., Arora, N., Kumar, R., Alvi, F. S., and Naughton, J. W., "Skin Friction Measurements Using Oil Film Interferometry in a 3–D Supersonic Flowfield," *AIAA Journal*, Vol. 57, No. 4, 2019, pp. 1373–1382.

[7] Lunte, J., and Schülein, E., "Wall Shear Stress Measurements by White-Light Oil-Film Interferometry," *Experiments in Fluids*, Vol 61, No:84, 2020,

[8] Greenblatt, D., Paschal, K. B., Yao, C. S., Harris, J., Schaeffler, N. W., and Washburn, A. E., "Experimental Investigation of Separation Control Part 1: Baseline and Steady Suction," *AIAA Journal*, Vol. 44, No. 12, 2006, pp. 2820-2830.

[9] Koklu, M., "Steady and Unsteady Excitation of Separated Flow over the NASA Hump Model," 2018 Flow Control Conference, AIAA Paper 2018-4016, 2018.

[10] Koklu, M., "Application of Sweeping Jet Actuators on the NASA Hump Model and Comparison with CFDVAL2004 Experiments," AIAA Paper 2017-0123, June 2017.

[11] Koklu, M., and Owens, L. R., "Comparison of Sweeping Jet Actuators with Different Flow-Control Techniques for Flow-Separation Control," *AIAA Journal*, Vol. 55, No. 3, 2017, pp. 848–860.

[12] Zigunov, F., Sellappan, P., and Alvi, F. S., "Flow Topology of the Slanted Cylinder Afterbody," AIAA Paper 2019-1141, 2019.
[13] Hough, P.V.C., "Method and Means for Recognizing Complex Patterns," US. Patent 3069654, 18 December 1962.
[14] Duda, R.O., and Hart, P.E., "Use of the Hough Transformation to Detect Lines and Curves in Pictures," *Communications of the ACM*, Vol. 15, No. 1, January 1972, pp. 11-15.
[15] Ballard, D.H., "Generalizing the Hough Transform to Detect Arbitrary Shapes," *Pattern Recognition*, Vol. 13, No. 2, 1981,
[16] Garcia D., "A Fast All-In-One Method for Post-Processing of PIV Data," *Experiments in Fluids*, Vol. 50, No. 5, Oct. 2010, pp. 1247-1259.
[17] Kuchment, P., "The Radon Transform and Medical Imaging," Society for Industrial and Applied Mathematics, 2013.
[18] van Ginkel, M., Luengo Hendriks C. L., and van Vliet L. J., "A Short Introduction to The Radon and Hough Transforms and How They Relate To Each Other". The Quantitative Image Group Technical Report Series, N. QI-2004-01, pages 1–9, 2004.
[19] Grayver, A.V., and Noir, J., "Particle Streak Velocimetry Using Ensemble Convolutional Neural Networks.", *Experiment in Fluids*, Vol.61, No.38, 2020.
[20] https://github.com/agrayver/streakcnn
[21] Naughton J. W., and Liu T., "Photogrammetry in Oil-Film Interferometry", *AIAA Journal*, Vol.45, No.7, pp:1620–1629, July 2007.
[22] Naughton, J. W., Viken, S., and Greenblatt, D., "Skin Friction Measurements on The NASA Hump Model," *AIAA Journal*, Vol. 44, No.6, pp. 1255–1265, June 2006.
[23] Greenblatt, D., and Washburn, A., "Influence of Finite Span and Sweep on Active Flow Control Efficacy", *AIAA Journal*, Vol. 46, No. 7, 2008, pp. 1675–1694.

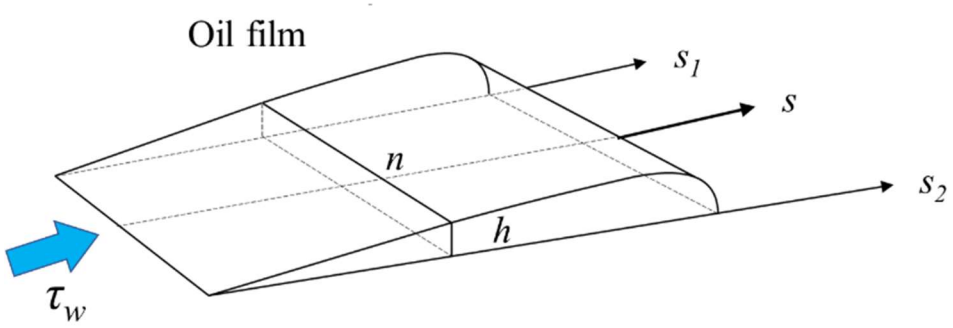

Fig. 1 Oil film under the effect of wall shear stress.

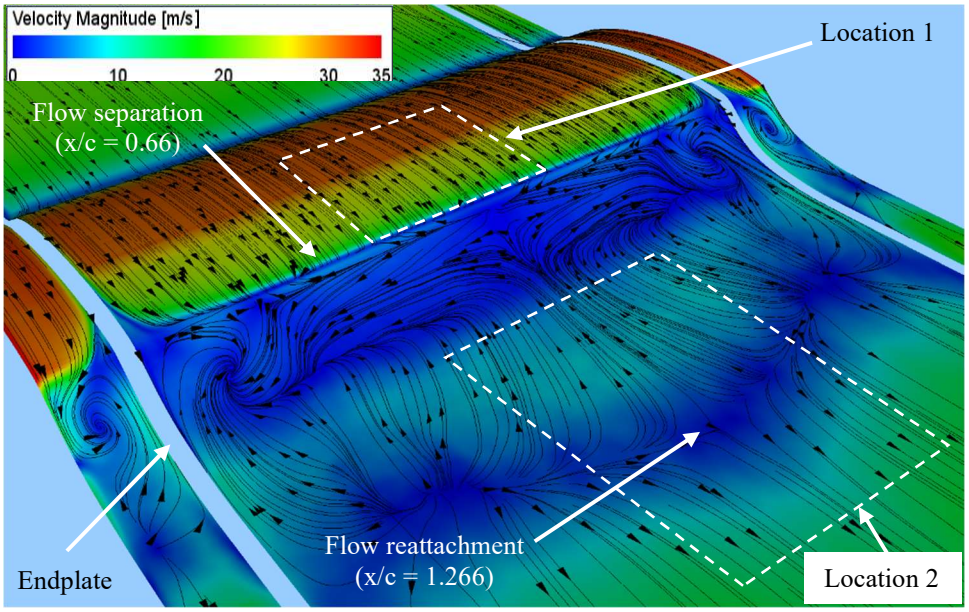

Fig. 2 Numerical surface flow visualization of the separated flow on the hump model [9]. Location 1 and Location 2 correspond to two locations that the surface flow vector extraction method was applied.

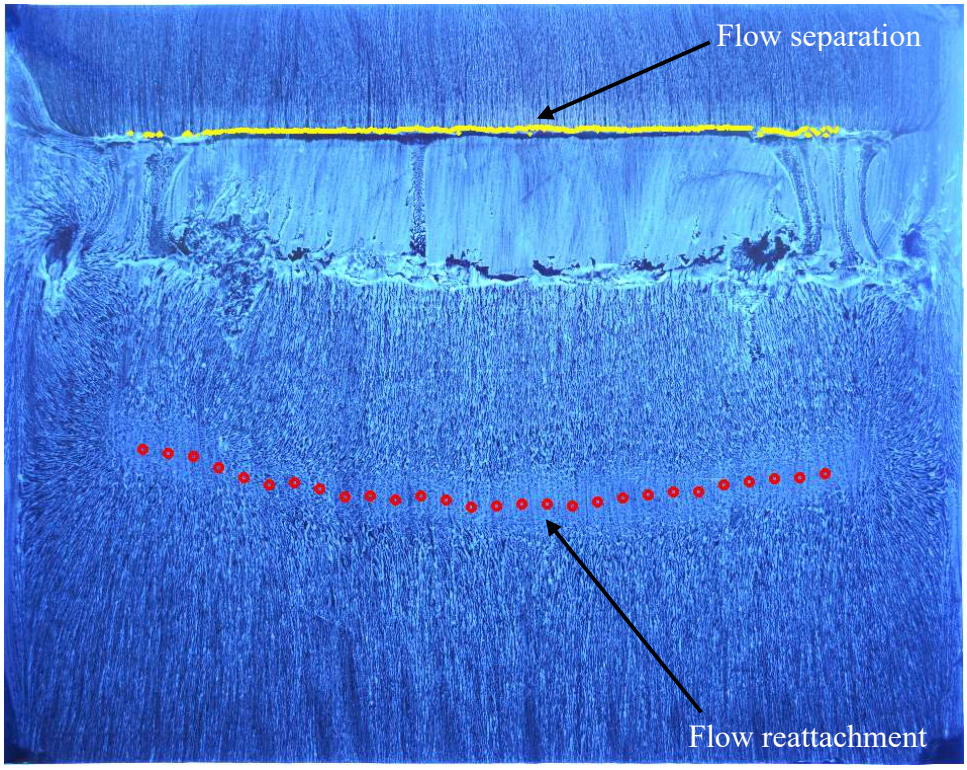

Fig. 3 Surface oilflow visualization of the separated flow on the hump model [10].

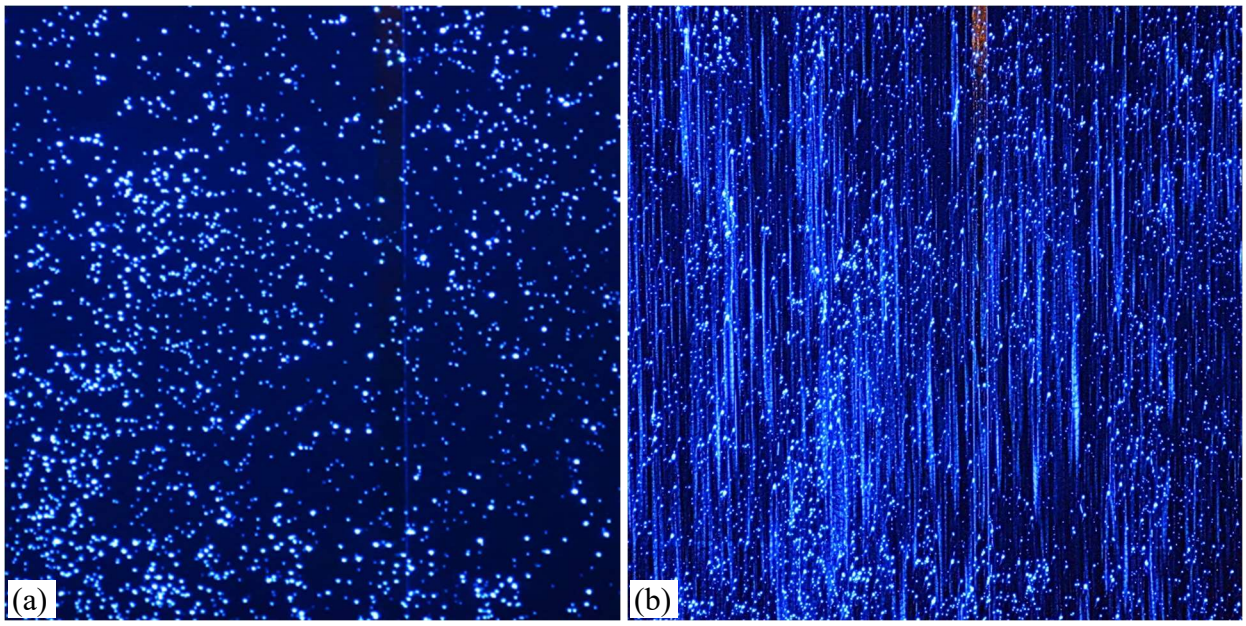

Fig. 4 (a) Fluorescent particles before wind on and (b) oil streaklines after wind on.

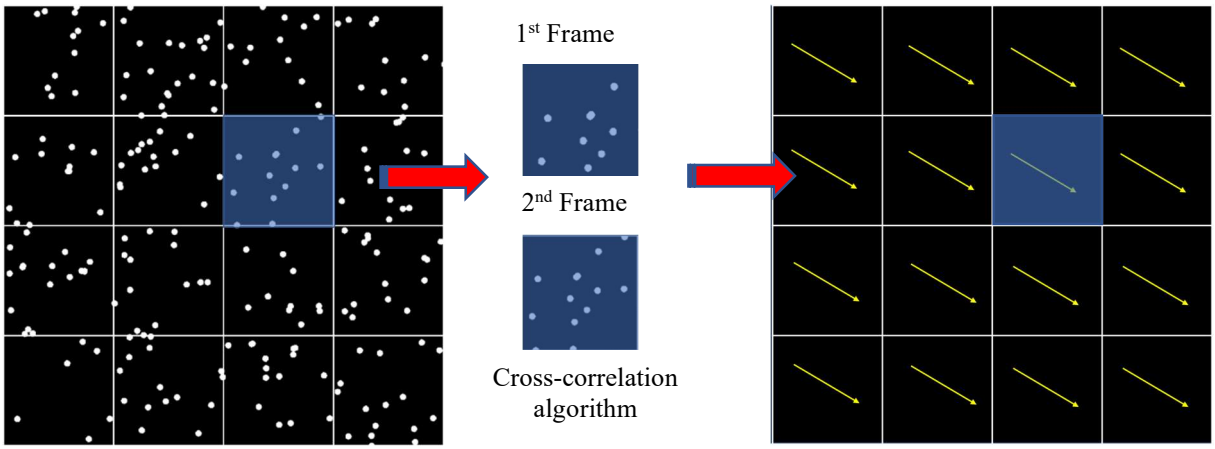

Fig. 5 Working principle of particle image velocimetry, PIV.

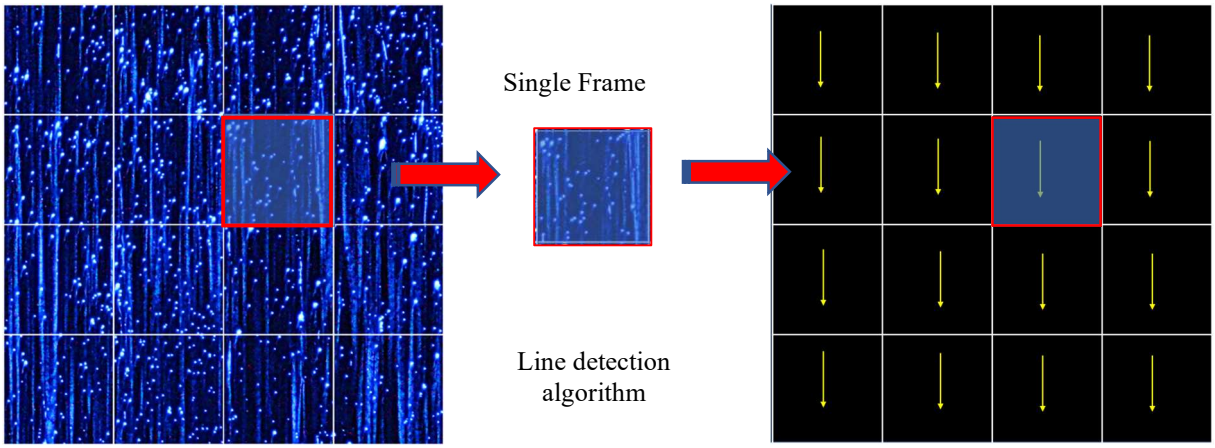

Fig. 6 Working principle of surface flow vector extraction method, SFVE.

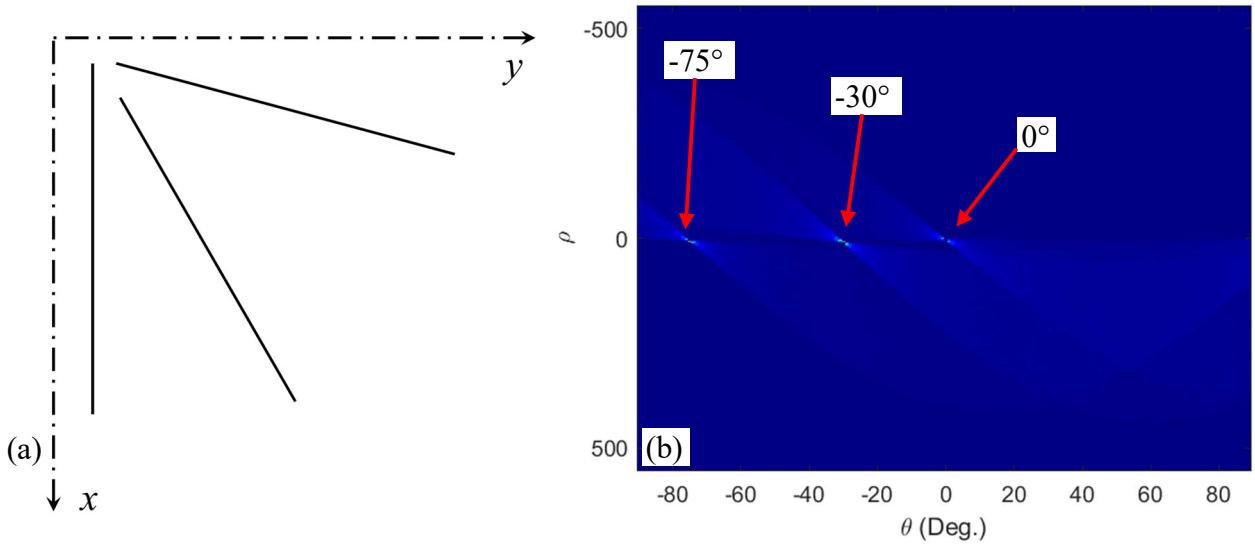

Fig. 7 (a) A sample input image with three lines and (b) rendering of Hough transform.

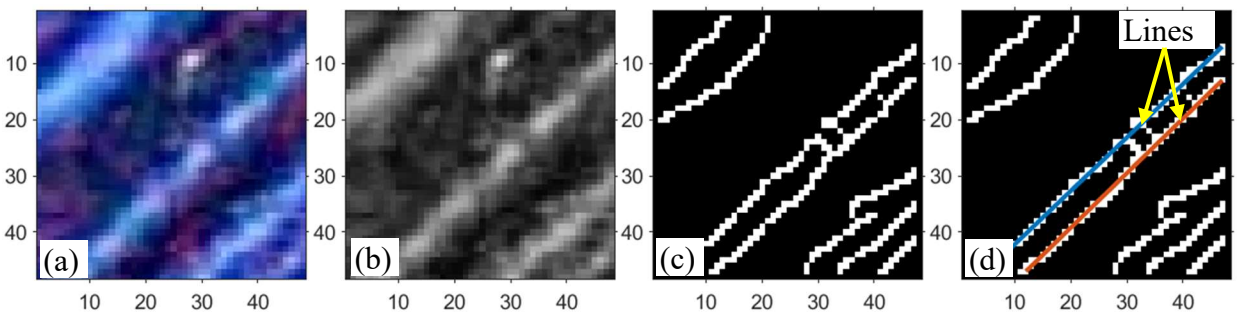

Fig. 8 Image procession sequence of an (48 px X 48 px) interrogation window for surface flow extraction: (a) raw image, (b) grayscale image, (c) edge detection, and (d) line (i.e., flow vector) detection.

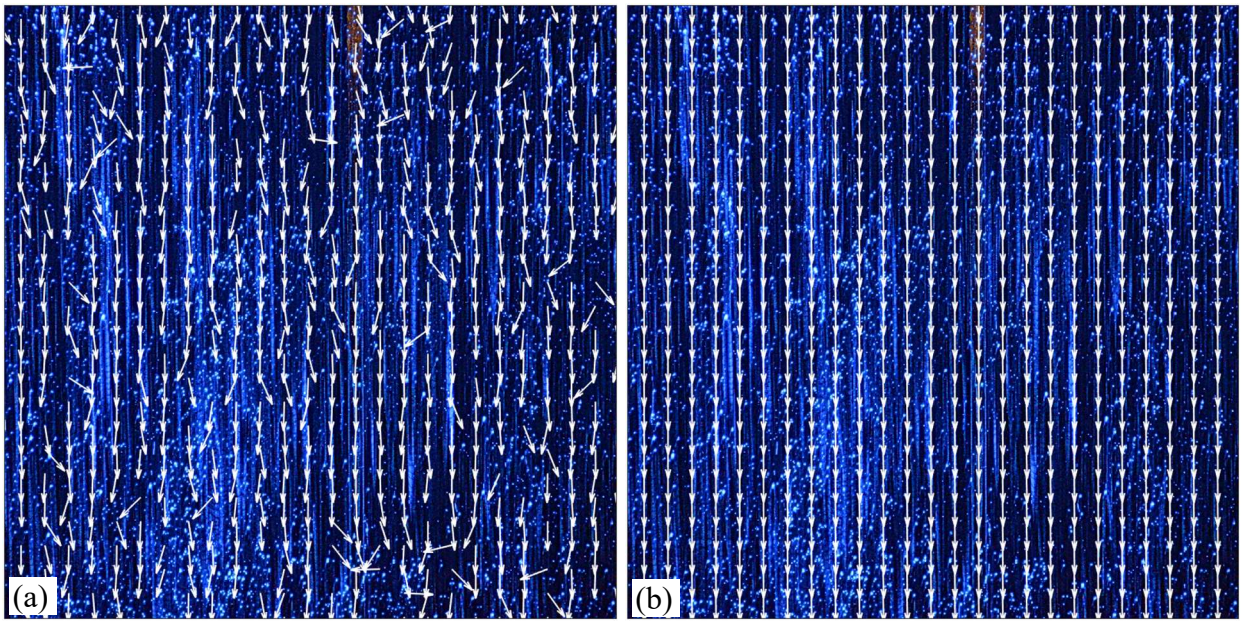

Fig. 9 Surface flow vectors overlaid on the OFV image (a) raw vectors and (b) postprocessed vectors.

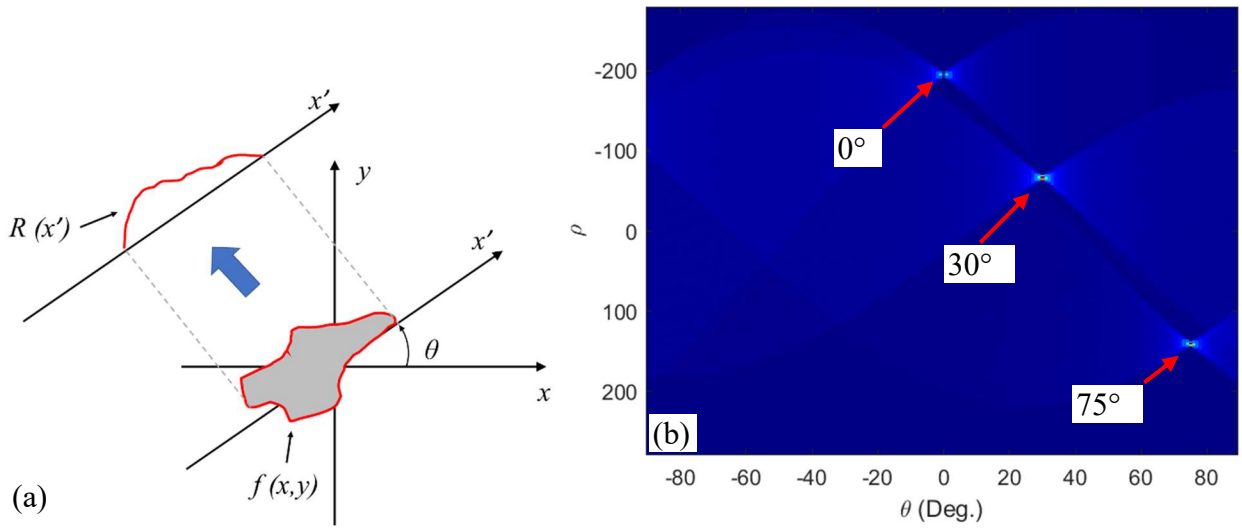

Fig. 10 (a) Mapping of Radon transform and (b) rendering of Radon transform with input image in Fig. 7a.

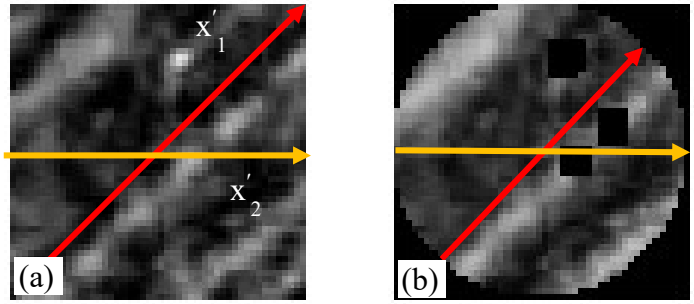

Fig. 11 Integral lines x_1' and x_2' in (a) a rectangular and (b) a circular interrogation window.

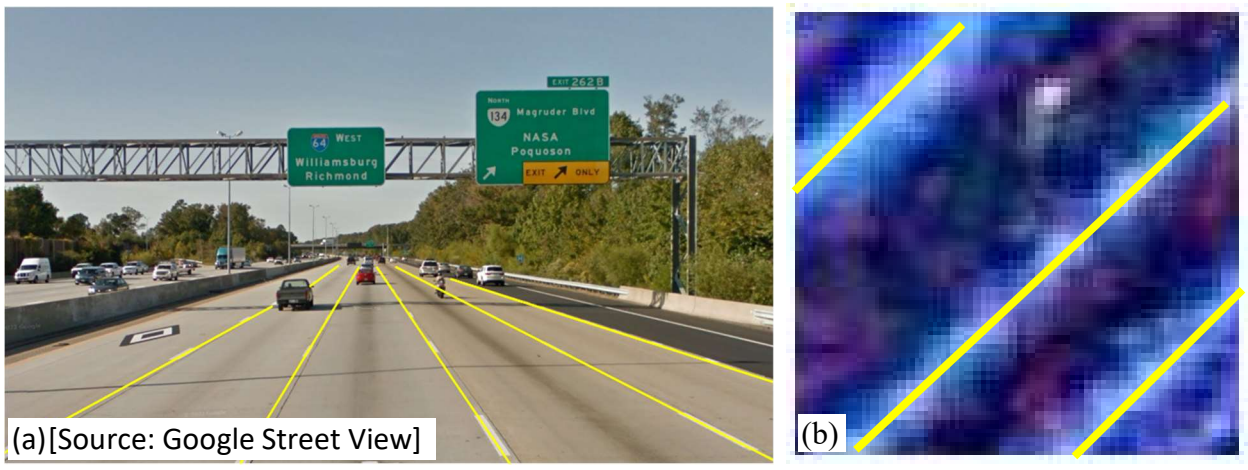

Fig. 12 Machine learning for (a) road lane detection and (b) oil streakline detection.

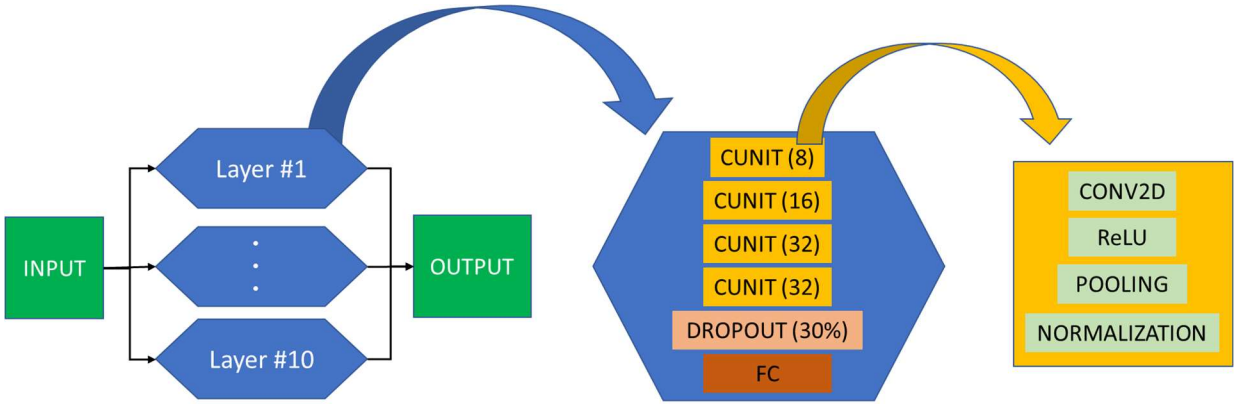

Fig. 13 Architecture of the CNN algorithm used.

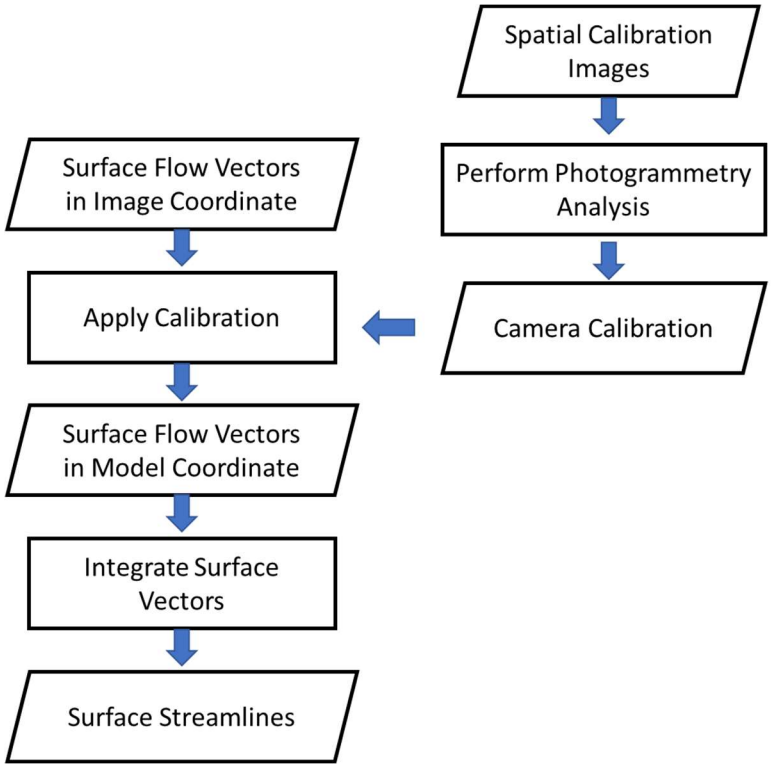

Fig. 14 Process used to determine surface streamlines from surface flow vectors.

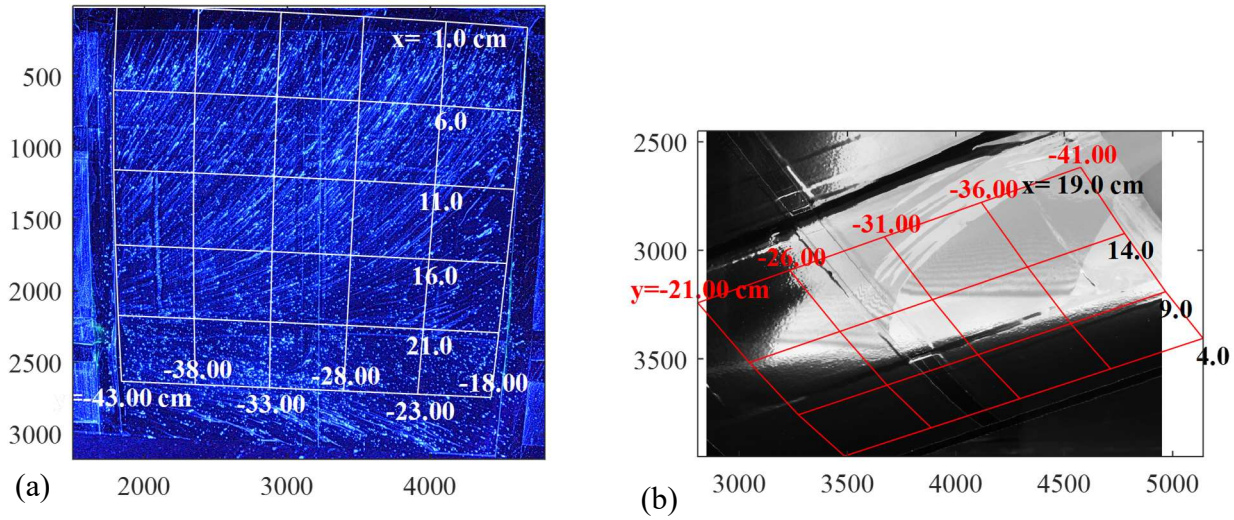

Fig. 15 Sample images with different camera settings are shown with the model and image coordinates: (a) oilflow visualization image and (b) oilfilm interferometry image.

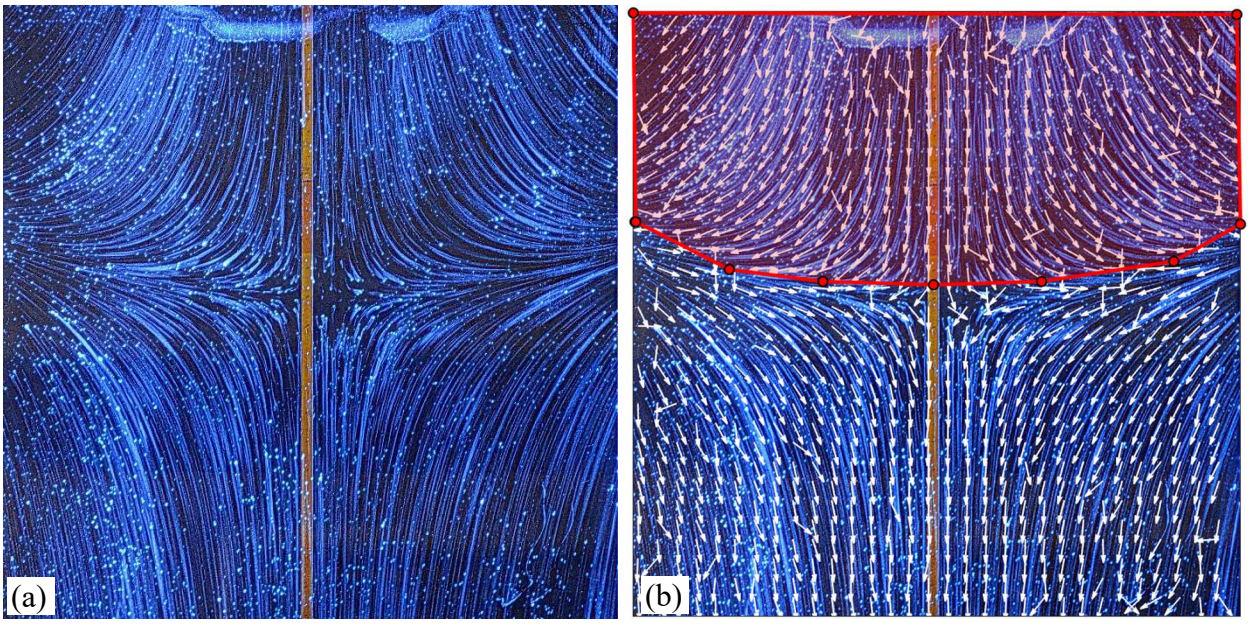

Fig. 16 (a) Surface oilflow visualization and (b) extracted surface flow vectors at location 2 in Fig. 2.

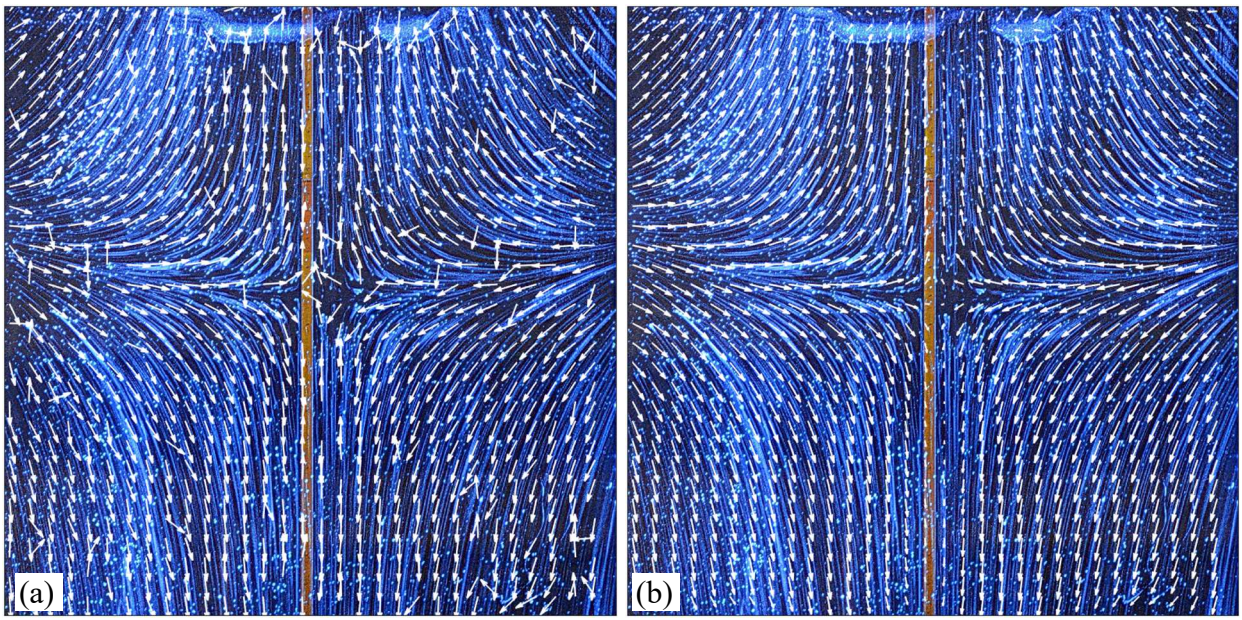

Fig. 17 (a) Corrected surface flow vectors and (b) postprocessed surface flow vectors.

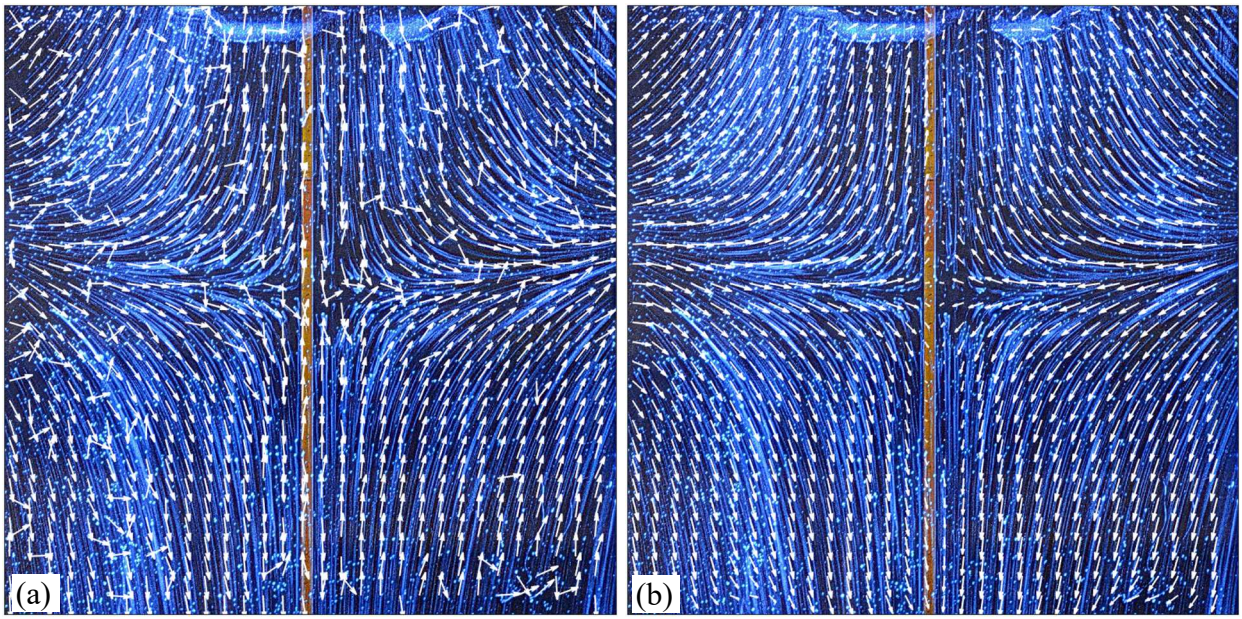

Fig. 18 (a) Raw vector field obtained using Radon transformation and (b) postprocessed vector field.

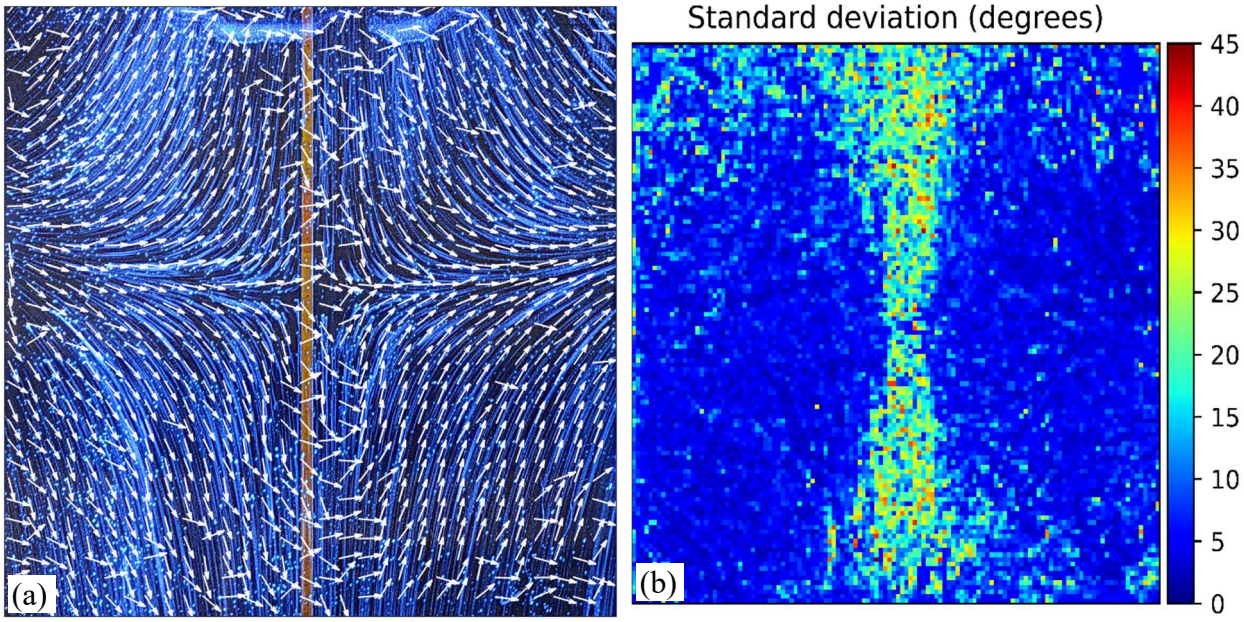

Fig. 19 (a) Raw vector field obtained using CNN and (b) standard deviation of flow direction angles.

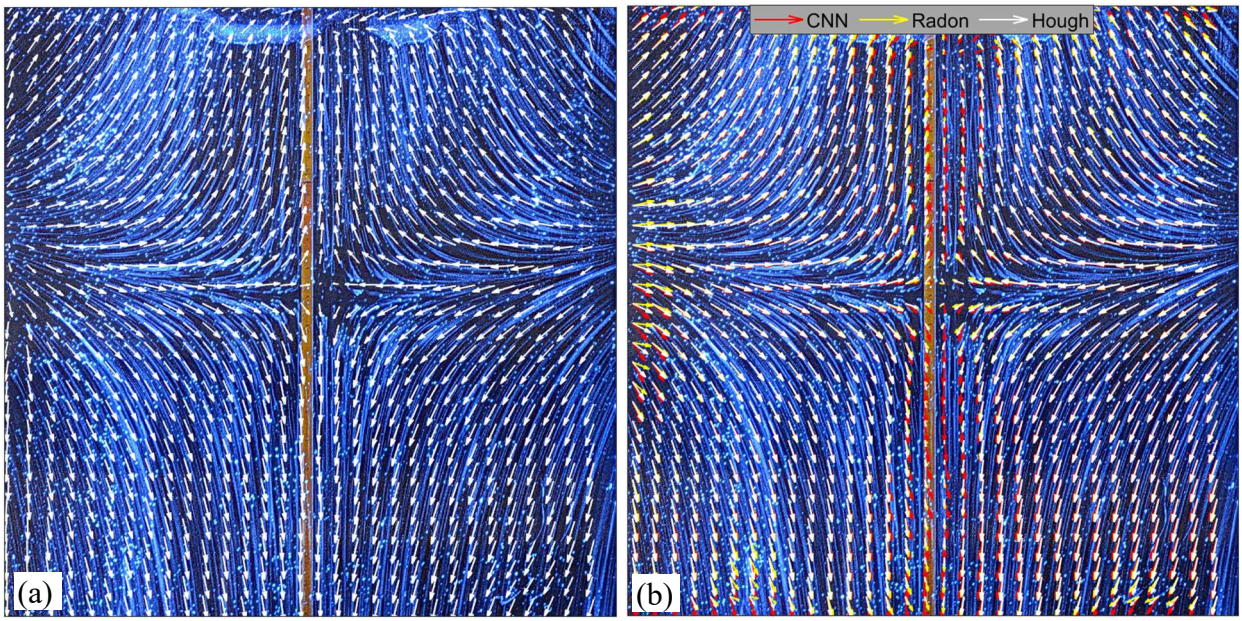

Fig. 20 (a) Postprocessed vector field using the CNN algorithm and (b) comparison of the vector fields obtained with different line detection algorithms.

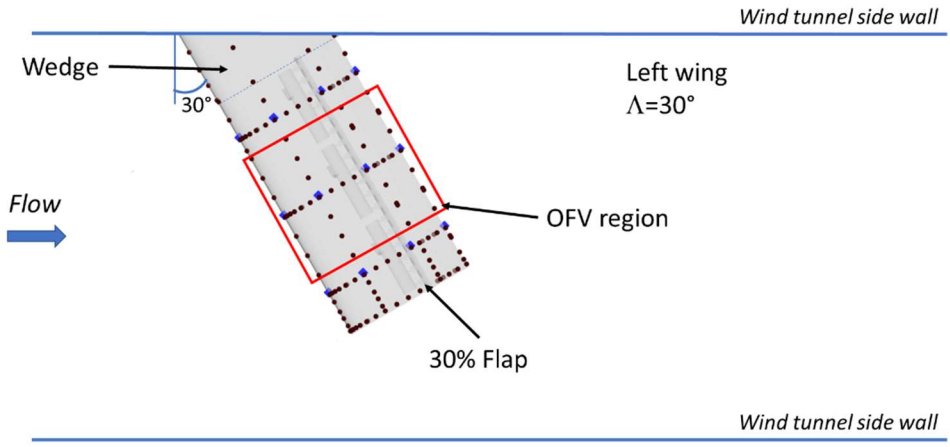

Fig. 21 3D NACA 0015 model setup in the wind tunnel.

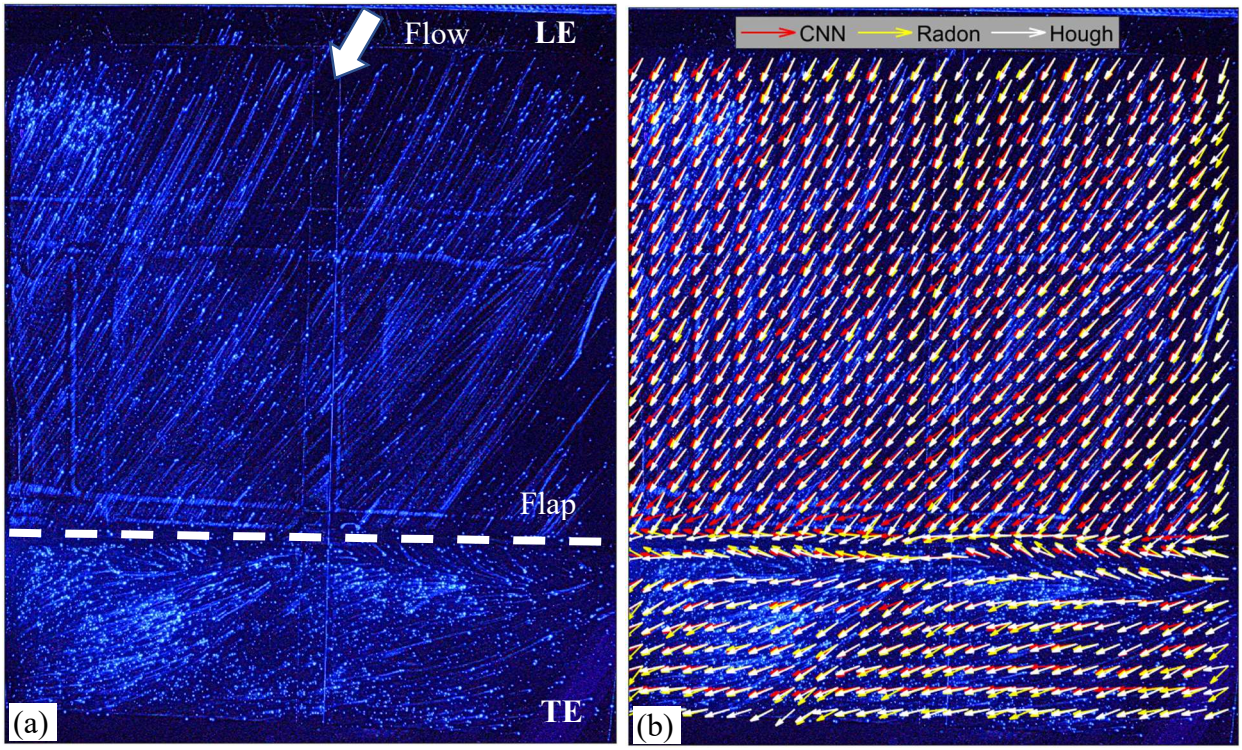

Fig. 22 (a) Surface oilflow visualization on the NACA 0015 model at α = 8° and (b) comparison of the vector fields obtained using three different line-detection algorithms.

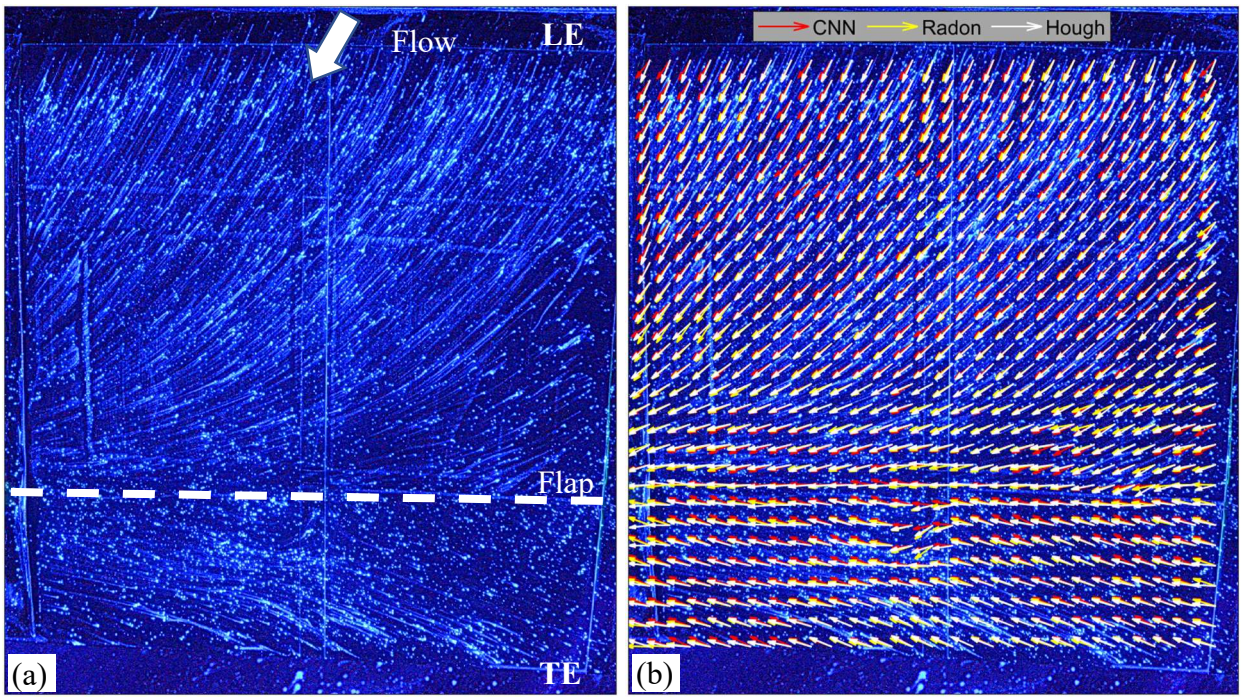

Fig. 23 (a) Surface oilflow visualization on the NACA 0015 model at α = 14° and (b) comparison of the vector fields obtained using three different line-detection algorithms.

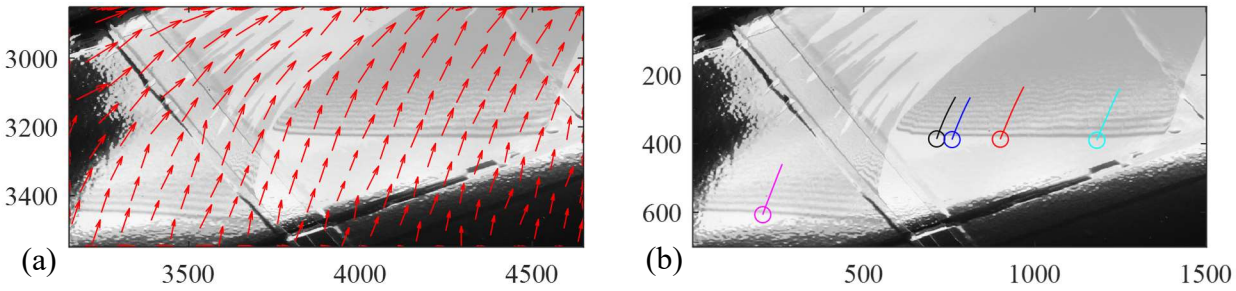

Fig. 24 Interferograms shown with (a) surface flow vectors and (b) surface streamlines determined by integrating the flow vectors. The symbols indicate the location where the surface streamlines were started.

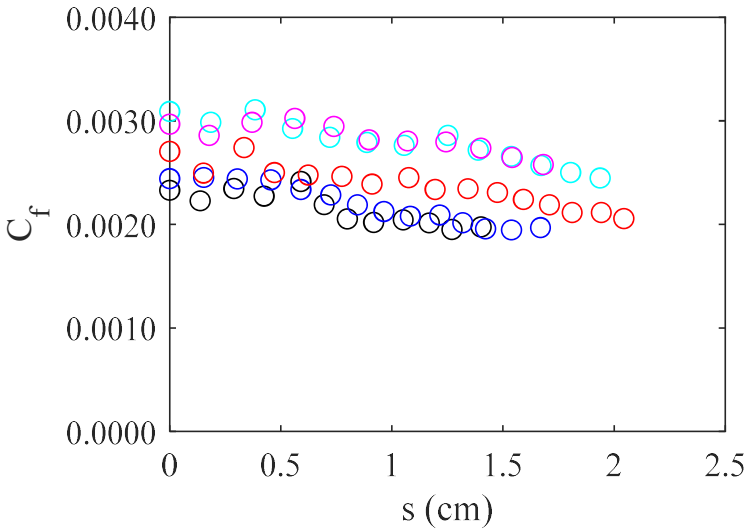

Fig. 25 – Skin friction coefficient along the lines shown in Fig. 24b. The symbol colors relate to the line colors in Fig. 24b for which the skin friction is determined.